

Available online at www.sciencedirect.com

jmr&t
Journal of Materials Research and Technology
journal homepage: www.elsevier.com/locate/jmrt



Original Article

Modelling and optimization of microhardness of electroless Ni–P–TiO₂ composite coating based on machine learning approaches and RSM



Imtiaz Ahmed Shozib^{a,*}, Azlan Ahmad^a, Md Shokor A. Rahaman^b,
Ahmad majdi Abdul-Rani^a, Mohammad Azad Alam^a,
Mohammadali Beheshti^{a,c}, Iqbal Taufiqurrahman^a

^a Mechanical Engineering Department, Universiti Teknologi PETRONAS, Seri Iskandar, 32610, Perak, Malaysia

^b Shale Gas Research Group, Institute of Hydrocarbon Recovery, Universiti Teknologi PETRONAS, Seri Iskandar, 32610, Perak, Malaysia

^c Centre for Corrosion Research, Universiti Teknologi PETRONAS, Seri Iskandar, 32610, Perak, Malaysia

ARTICLE INFO

Article history:

Received 13 January 2021

Accepted 13 March 2021

Available online 20 March 2021

Keywords:

Microhardness

Electroless Ni–P–TiO₂ coating

Response surface methodology

Artificial neural network

Random forest

Extra trees

ABSTRACT

In this study, experimental investigations on the microhardness of the synthesized electroless Ni–P–TiO₂ coated aluminium composite was carried out. The coated samples were characterized by scanning electron microscopy (SEM) for surface morphology and X-ray diffraction (XRD) pattern for phase recognition. The microhardness of the electroless Ni–P–TiO₂ coated composite was measured and predicted by various machine learning algorithms. The recorded datasets were used for optimization by Response Surface Methodology (RSM) model whereas, training and testing of the four different Artificial Intelligence (AI) models were executed using machine learning methods. The four AI models applied in this study were Support Vector Machine (SVM), Artificial Neural Network (ANN), Random Forest (RF) and Extra Trees (ET). The objective of this analysis was to quantify the accuracy of microhardness prediction of four types of AI models along with RSM model. The obtained results revealed that the extra trees (ET) model showed outstanding performance amongst the five models for training, testing, and overall datasets with coefficient of correlation (R^2), MSE and MAE value of 94.47, 75.38 and 4.67, respectively. This analysis therefore recommends the ET model in the prediction of microhardness of electroless Ni–P–TiO₂ composite coating due to its superior and robust performance.

© 2021 The Authors. Published by Elsevier B.V. This is an open access article under the CC BY-NC-ND license (<http://creativecommons.org/licenses/by-nc-nd/4.0/>).

1. Introduction

Electroless Ni–P coating is a notable surface modification technique which has been widely used in mechanical,

chemical, and electronic industries due to their enhanced microhardness and wear resistance [1]. In recent years, the integration of nano-sized particles into Ni–P matrix coatings has tremendously improved their properties. To improve the mechanical and tribological properties, different types of

* Corresponding author.

E-mail address: imtiazshozib87me@gmail.com (I.A. Shozib).

<https://doi.org/10.1016/j.jmrt.2021.03.063>

2238-7854/© 2021 The Authors. Published by Elsevier B.V. This is an open access article under the CC BY-NC-ND license (<http://creativecommons.org/licenses/by-nc-nd/4.0/>).

nanoparticles have been used to integrate into the Ni–P matrix, such as Ni–P–Ag [2], Ni–P–SiC [3], Ni–P–SiO₂ [4], Ni–P–Si₃N₄ [5], Ni–P–Al₂O₃ [6], Ni–P–TiO₂ [7,8]. Titanium dioxide (TiO₂) has retained its appeal as an incorporating nanomaterial in electroless Ni–P composite matrix due to possessing the outstanding features of microhardness and corrosion resistance [7,9]. Aluminium alloy is one of the most widely used alloys in industrial applications due to its outstanding physical, chemical and tribological properties. They are mainly used for food additives, beverages cans, cooking utensils, surgical instruments, and aircraft structural applications [10–12]. Although aluminium alloys have numerous advantages and applications, they have one major drawback that is they possess significantly low microhardness compared to other metals. Microhardness is one of the most relevant and broadly studied mechanical properties for structural assessment. In order to control wear and tear processes, surface hardness is particularly important for use in components and semifinished goods. This makes hardness a property of materials that assess the protection and safety of industrial appliances. To improve the hardness of aluminium alloy, electroless Ni–P–TiO₂ composite coating can play a vital role. The present study examines the reliance on different bath compositions and coating process parameters on the hardness characteristics of the electroless Ni–P–TiO₂ composite coating.

The precision, repeatability, and correlation problems are ingrained in microhardness testing. This is due to the fact that the microhardness measurement is based on the length of the diagonals of the diamond indenter and the range of diagonal length values is very sensitive to the precision of micrometres. Therefore, identifying the location of the indent tips is the main challenge because it requires proper illumination, calibration of the optics for optimum resolution, and proper focusing to get acceptable image quality. It can produce erroneous results if not illuminated and magnified properly. This raised the indentation size effect (ISE) problem, referring to the fact the test results on a material are not constant over the range of test loads [13,14]. Moreover, multi-dimensional and non-linear relationship emerge between the operational coating parameters (input) and microhardness (output) which cannot lead to extract accurate analytical formulation for further usage. In addition, it is time consuming and expensive to experimentally evaluate the microhardness of the substrate. Such cost, time losses and complexities can be minimized by utilizing RSM and machine learning algorithms.

Design of experiment (DOE) is an effective numerical and statistical technique to solve complicated and multifactor engineering problems, prompted with a need to reduce the number of experiments, costs, time and physical efforts. The Response Surface Methodology (RSM) is a highly advanced DOE method that includes statistical formulation for model creation and process analysis aimed at optimizing the desired response managed by multiple input parameters [15,16]. RSM enables the development of a polynomial function that relates to the response and interaction of process variables [17]. The most extensively used response surface is the central composite design (CCD), which provides considerable optimization for most of the stable processes.

The use of machine learning algorithms in the field of material science has improved the manufacturing process of

new materials for a broad array of applications over the last decade. Recently, AI models have been appeared as an important tool to explore the relations to a target property between material attributes, including compositional, elemental, and structural [18]. The key concept of machine learning is to learn useful patterns from previous data and with the help of the mapping data it can generate rigorous model. The prognostication of any material property can be improved by several orders of magnitude through machine learning approaches. Machine learning has a good applicability in regression analysis with high dimensional data and thus plays an important role to predict fundamental properties such as hardness [19], formation energies [20], thermal conductivity [21] and glass transition temperature [22] in the field of materials science. Furthermore, machine learning is also being used for solving the complicated problems including phase predictions and surface roughness of different materials [23,24]. If machine learning algorithms are implemented as essential methods for precisely predicting microhardness, enormous amounts of time and experimental resources invested in testing microhardness can be saved [25]. Therefore, there is in urgent need to develop high-performance AI models that can precisely predict the microhardness response of the composites with little effort and in a small space of time.

Several researchers already adopted machine learning approaches to predict fundamental properties of electroless Ni–P coating. Yating et al. [26] predicted the plating rate and phosphorus content of electroless Ni–P coating based on Ni²⁺/H₂PO₂, complexing agent, stabilizer, pH and temperature as input parameters. H. Beygi et al. [27] also predicted the plating rate of electroless Ni–P coating based on the coating compositional parameters. Vaghefi et al. [28] predicted the phosphorus content (wt.%) in electroless Ni–P coating considering pH, metal turnover (MTO) and bath loading as input parameters. Zou et al. [29] established PSO-BP (Particle Swarm Optimization-Back Propagation) model to predict the phosphorus content of electroless Ni–P coating considering temperature, pH, sodium hypophosphite concentration, and lactic acid concentration as the input parameters. The above-mentioned researchers applied the artificial neural network in predicting the plating rate and phosphorus content of electroless Ni–P coating. From above mentioned literature, microhardness prediction by machine learning algorithms of electroless Ni–P–TiO₂ composite coating has remained unaddressed. Heretofore, there is still no detailed framework of machine learning algorithms that illustrates the impact on microhardness of the plating bath composition and coating process parameters. However, there are few papers on the use of statistical optimization tool to predict the microhardness of electroless Ni–P coating [30–32]. Many researchers recommend the use of machine learning algorithms rather than statistical tools to predict mechanical properties where the relationships between input parameters and outcome are non-linear [33,34]. It is due to the fact that machine learning is inherently more capable of capturing these non-linear relationships than statistical optimization tools.

In the present study, the experimental investigation has been done by depositing coating on the substrates. The microhardness of the substrates was measured by Vickers

Table 1 – Compositions and operation conditions of electroless plating bath solutions.

Composition	Ni–P	Ni–P–TiO ₂
Nickel sulphate hexahydrate (NiSO ₄ ·6H ₂ O)	40, 50 gm/L	40, 50 gm/L
Sodium hypophosphite monohydrate (NaH ₂ PO ₂ ·H ₂ O)	30, 35 gm/L	30, 35 gm/L
Sodium citrate dihydrate (Na ₃ C ₆ H ₅ O ₇ ·2H ₂ O)	30 gm/L	30 gm/L
Thiourea (CH ₄ N ₂ S)	2 mg/L	2 mg/L
Titanium dioxide (TiO ₂)	0 gm/L	2, 5 gm/L
pH	4.8–5.2	4.8–5.2
Time	60–120 min	60–120 min
Temperature	80–95 °C	80–95 °C
Stir	100 rpm	100 rpm

Microhardness tester. To recognize the microstructure features of electroless Ni–P–TiO₂ composite coating, the characteristics of the coating was identified with the aid of SEM surface morphology, EDS and XRD pattern. The main objective of this work is to accurately model and predict Vickers microhardness of electroless Ni–P–TiO₂ composite coating from coating operational parameters and coating compositions for accelerating the determination process of Vickers microhardness of electroless Ni–P–TiO₂ composite coating. RSM model has been developed which considers a rigorous correlation of parameters, analyses interactions between independent variables, optimizes them and provides the overall effect of variables on microhardness of the Ni–P–TiO₂ composite coating. To state of the art, the AI models have been introduced to predict microhardness of the developed composites with different machine learning approaches. The machine learning approaches namely- Support Vector Machine (SVM), Artificial Neural Network (ANN), Random Forest (RF), and Extra Trees (ET) have been applied as a novel approach by using the database collected from coating operational parameters. These strategies of machine learning approaches have not been reported anywhere else to predict the accurate microhardness of developed composites and compared among them based on the performance metrics. The four AI models were compared with the RSM model by evaluation parameters.

2. Materials and methods

2.1. Coating preparation and deposition

Commercial Aluminium alloy was used as the substrate and each sample had a dimension of 20 × 20 × 3 mm³. A sequence of pre-treatment procedures prior to plating was carried out in order to achieve proper coating deposition on the substrate. The specimens were manually polished to a grit of 800 using SiC abrasive paper, then ultrasonically degreased in acetone for 5 min. The pre-treatment procedures for the substrates before immersion in electroless plating bath solution required washing for 3 min in a 50 gm/L NaOH solution and etching for 1 min at room temperature using 300 gm/L HNO₃ solution. Subsequently, each specimen was submerged in distilled

water for 2 min. This experiment utilizes a typical electroless Ni–P plating bath solution including Nickel sulphate hexahydrate (NiSO₄·6H₂O) as the main salt, Sodium hypophosphite monohydrate (NaH₂PO₂·H₂O) as the reducing agent and sodium citrate dihydrate (Na₃C₆H₅O₇·2H₂O) as the complexing agent. To agitate the electroless plating bath solution continuously and prevent unnecessary agglomeration of nanoparticles, a magnetic stirrer was used. The coating compositions and electroless plating bath conditions are stated in Table 1.

The images (Fig. 1) reveal the coated substrates of electroless Ni–P and Ni–P–TiO₂ composite coating.

2.2. Coating characterization

A Scanning Electron Microscopy (ZEISS EVO LS15 VPSEM) was used to analyse the surface morphology of the electroless Ni–P and electroless Ni–P–TiO₂ coated samples. The elemental distribution of coating composition was identified from Energy Dispersive Spectroscopy (EDS) in terms of weight percentage (wt.%). In order to identify the phase structure of the coating compositions and confirm the presence of nanoparticles, the X-ray diffractometer (D8 ADVANCE, Bruker AXS Inc., USA) was used. The X-ray Diffraction (XRD) pattern of the coated sample was recorded applying CuKα (1.5406 Å) radiation with 40 mA current and 45 kV operating voltage at 25 °C temperature.

2.3. Microhardness measurement

The microhardness of Ni–P and Ni–P–TiO₂ coated samples was tested according to the standard test method (ASTM E92-82). Vickers hardness tester (LM-247 AT) was used by applying a load of 100 gf for 10 s on the substrates. The hardness measurement was conducted three times for each sample at different locations, and mean values were taken into consideration for microhardness.

2.4. Experimental design

The datasets for the construction of RSM and AI models were collected from our own orthogonal experiments scheme. Considering the main factors NiSO₄, NaH₂ PO₂, TiO₂, Time, Temperature orthogonal experiment scheme

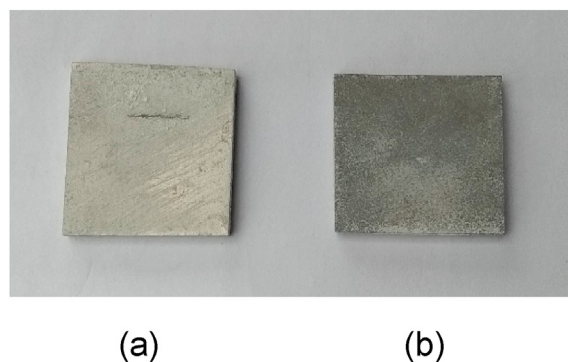


Fig. 1 – The appearance of (a) Ni–P and (b) Ni–P–TiO₂ coating on aluminium plate.

Table 2 – Orthogonal experiments scheme of the main factors $L_{36} (2^2, 3^3)$.

Level	Factor				
	NiSO ₄ (gm/L)	NaH ₂ PO ₂ (gm/L)	TiO ₂ (gm/L)	Time (minutes)	Temperature (°C)
1	40	30	0	60	80
2	50	35	2	90	87
3	—	—	5	120	95

was designed, as shown in Table 2. In both cases for AI and RSM models, two different levels of process parameters (NiSO₄, NaH₂PO₂) and three different levels of process parameters (TiO₂, Time, Temperature) were selected. Three different coating temperatures were selected as one of the process variables to observe the effect of different temperatures on microhardness response. The different temperatures were in the range of previously reported literature [26,35,36]. The coating compositions were decided on the basis of existing literature of electroless Ni coating [37–39]. Total 36 runs were suggested by “Minitab” software to optimize the response.

2.5. Machine learning approaches

Python 3.7.2 with libraries of scientific computing such as pandas 0.19.2 and NumPy 1.12.1 providing pre-processing methods and the efficient data structure has been used in this work for training the machine learning models. Again, scikit-learn has been imported for supporting the four machine learning models such as SVM ANN, RF and ET.

2.5.1. Support Vector Machine (SVM)

The standard SVM formulation is defined as a maximum margin classifier whose decision-making feature is a hyper-plane that distinguishes samples from different classes to the maximum possible extent. The SVM method can solve the following equations from a labelled training dataset set $\{x_i, y_i\}_{i=1}^n$, where $x_i \in \mathbb{R}^N$ and $y_i \in \{-1, +1\}$, and given a nonlinear mapping $\varphi(\cdot)$.

$$\min_{w, \xi_i, b} \left\{ \frac{1}{2} \|w\|^2 + C \sum_{i=1}^n \xi_i \right\} \quad (1)$$

constrained to:

$$y_i(\varphi(x_i), w + b) \geq 1 - \xi_i \quad \forall i = 1, \dots, n \quad (2)$$

$$\xi_i \geq 0 \quad \forall i = 1, \dots, n \quad (3)$$

where w and b describe a linear classifier in \mathbb{R}^N since x_i is in \mathbb{R}^N and ξ_i are positive slack variables that allow permissible errors to be dealt with (Fig. 2). Notice that functional minimization involves two concepts with a simple meaning: it is aimed to minimize the errors committed, $\sum_{i=1}^n \xi_i$, thus minimizing the model weight norm, $\|w\|^2$, which can be seen to be equal to optimizing the margin (class separation). It can be observed that it is possible only to increase the margin without giving any proper attention to committed errors. This will result in a maximum SVM margin. The training error problem is minimized by adding the slack variables, and the solution is called the soft-margin SVM.

2.5.2. Artificial neural network (ANN)

Artificial Neural Network is a soft computational platform that mimics the human mind's ability to use modes of logic and/or pattern recognition effectively. ANNs are found to learn from the interactions given by training data between input and output. It generalizes the output, making it ideal for non-linear problems where the main characteristics are judgment, knowledge, and surrounding circumstances [41–44]. ANN conducts its functions in various layers by linking neurons. ANN is basically split into single-layered neural networks and multi-layered networks. In a multi-layered neural network, there are usually three layers: the input layer, the hidden layer, and the output layer. Depending on the given input size and the relation between the input and response variable, the hidden layer can contain single or multiple layers. Initially, along with the output, the input is provided to the network and parameters such as the learning function, training function, transfer function, number of neurons, number of layers and network type are selected to optimize the given input. With the transfer function $F(X)$, the number of weighted inputs is processed and the output after processing is given by Eq. (4).

$$Y = F(X) = F\left(\sum_{i=1}^n (W_{ij}X_i + b_j)\right) \quad (4)$$

where W_{ij} is the weight corresponding to given input X_i and b_j [45]. Performance from a neuron is calculated by using an appropriate transfer function to convert its input. Functions for transition can be linear or non-linear. For non-linear relationships [46,47], sigmoidal functions are widely used. The

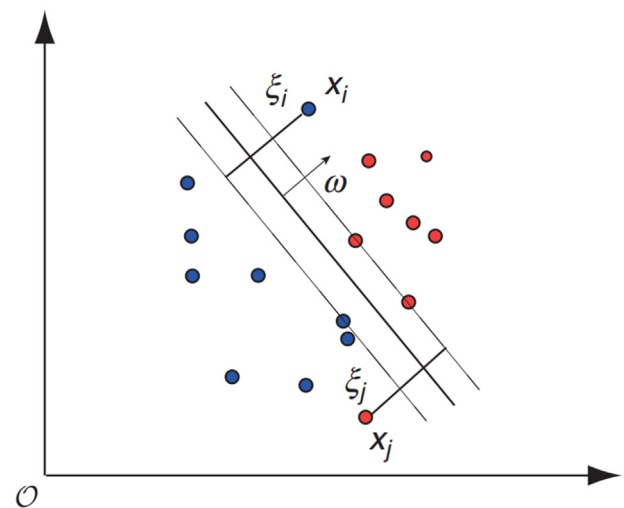


Fig. 2 – SVM: In a nonlinearly transformed, feature space, linear decision hyperplane where slack variables ξ_i are used to deal with errors [40].

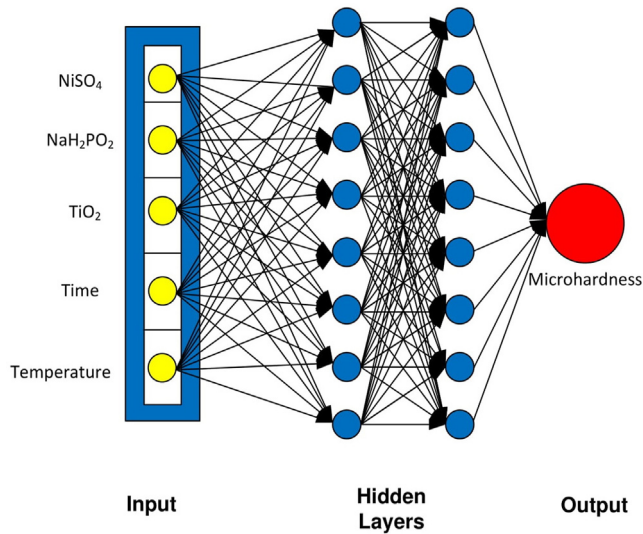


Fig. 3 – Neural network configuration (5-8-8-1) selected for microhardness prediction.

logarithmic sigmoid is the most common transfer function. The general nature of this function is defined as follows by Eq. (5).

$$F(X) = 1/(1 + e^{-x}) \quad (5)$$

For several forms of neural networks, Rectified Linear Unit (ReLU) has become the default activation function due to its better performance to train the model. The activation function of the Rectified Linear Unit (ReLU) observed in Eq. (6) does not require input data to be normalized.

$$g(x) = \max(0, x) \quad (6)$$

Finally, the validation data collection is used to test performance and helps prevent the issue of overfitting [44,48]. Four-layer architecture has been selected for the currently established ANN model (Fig. 3) for microhardness prediction.

2.5.3. Random forest (RF)

The use of algorithms for tree-based ensemble learning has achieved involvement in applications in different sectors and fields, such as agriculture [49], transportation [50], materials science [51], and energy [52]. Tree-based algorithms are especially known for producing practical and convenient performance [53,54]. In addition, these algorithms are effective because they maintain automatic interactions, even if large coefficients are available [54]. One of the tree-based ensemble techniques used for regression and classification is Random Forest (RF) [55]. Multiple decision trees are developed by a random subset of variables which is sorted and replaced independently from the original dataset [56]. Using a sequence of binary partitions (“splits”) on individual variables, these decision trees isolate the predictor space. The trees’ “root” node constitutes the complete predictor space. The non-split nodes are referred to as “terminal nodes” and construct the final partition of the predictor space. According to the value of one of the predictor variables, each non-terminal node splits into two descendant nodes, one on the left and one on the right. The data is separated into the two

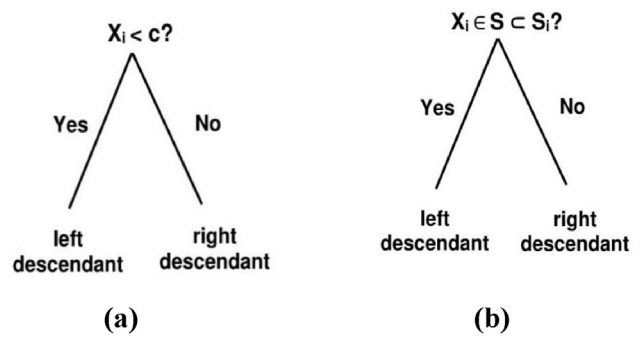


Fig. 4 – Splitting on a continuous predictor variable X_i , (a) using split point ‘c’ (b) using subset $S \subset S_i$ [57].

descendant nodes once a split has been chosen, and each of these nodes is classified in the same way as the original node.

If the split point ‘c’ is larger than predictor variable (X_i), then the variable will go to the left descendant and the rest will go to the right descendant (Fig. 4a). A predictor variable (X_i) captures values from a finite category $S_i = \{s_{i,1}, \dots, s_{i,m}\}$ set. A split sends a subset of these categories $S \subset S_i$ to the left and the remaining categories to the right (Fig. 4b). Until a stopping condition is imposed, the process continues sequentially. RF allows estimation of the relative value of input features, which is useful for reducing dimensionality to increase the efficiency of the model on high-dimensional datasets [58].

2.5.4. Extra trees (ET)

The ET technique is computationally efficient, like Random Forest (RF), and can deal with high-dimensional input vectors [59]. Extra tree (ET) uses the same concept as random forest (RF) and uses each base estimator to train a random subset of features. It chooses the best feature randomly, however, along with the corresponding value for dividing the node [60]. The entire training dataset is used by ET to train each regression tree that averages the Decision Trees (DTs) forecasts with higher accuracy [59,61]. Here, DTs are first shortly described as the basic development of the ET models.

The structure of DT has been shown in (Fig. 5). The source set is split into the first sub-set layer from the root node and is computed for the entire training dataset by using the splitting method. Each internal node belongs to the input parameter and performs a test on that input function, representing the test results as the branches that lead to the root-to-leaf path of the feature to the other internal nodes or terminal leaves. The target values of the leaf nodes are either a different expected outcome in classification trees or the average outcome of training data in regression trees. The leaves of the regression trees are classified by local sample averaging of the output variable with prediction values (\hat{y}_i) as follows [61]:

$$\hat{y}_i = \frac{1}{|L_j|} \sum_{(x^i, y^i): x^i \in L_j} y_i \quad (7)$$

where $|L_j|$ indicates the number of learning cases that access the leaf node L_j . The developed number of trees regulates how robustly the difference of the ensemble model aggregation is minimized [59]. ETs have greater computing effectiveness and prediction efficiency than single trees [61].

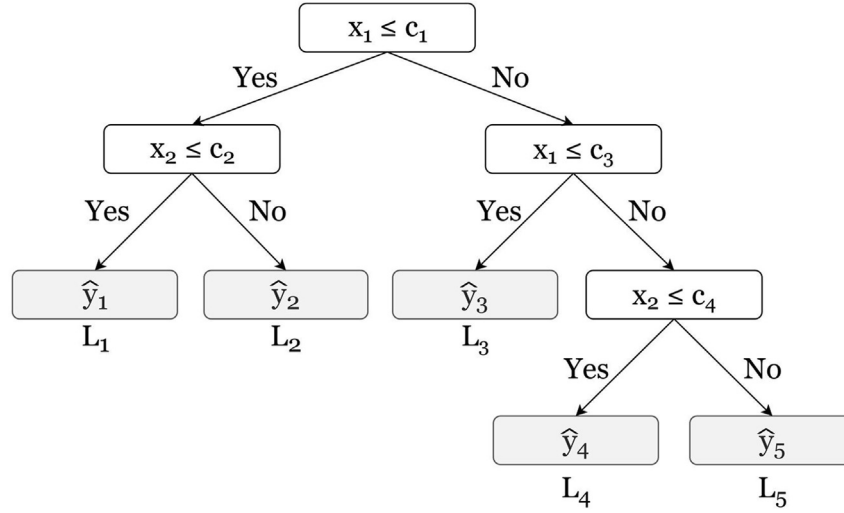


Fig. 5 – A sample of DT with two input variables (x_1 and x_2), cut points (c_i), and five leaf nodes (L_1, L_2, \dots, L_5) with target values ($\hat{y}_1, \hat{y}_2, \dots, \hat{y}_5$) [62].

2.6. Evaluation criteria for the AI models and RSM

An integral part of the process of developing machine learning models is the measurement of the model accuracy to explain how well the model performs in its predictions. The Mean Squared Error (MSE), Mean Absolute Error (MAE) and Correlation coefficient (R^2) are used primarily in regression analysis to determine the prediction error rates and model efficiency. The difference between the original and predicted values derived by the square average difference over the data set is expressed by the MSE. The discrepancy between the original and predicted values derived by the average absolute difference from the data set is defined by MAE. The R^2 value reflects the coefficient of how well the values match to the original values. The higher value of R^2 represents better AI models. The value from 0 to 1 interprets as percentages. The fitting errors of the training and prediction analyses from the various models have been tested based on MSE, MAE and R^2 calculated by Eq. (8), Eq. (9), and Eq. (10) respectively.

$$MSE = \frac{1}{N} \sum_{i=1}^N (y_i - \hat{y})^2 \quad (8)$$

$$MAE = \frac{1}{N} \sum_{i=1}^N |y_i - \hat{y}| \quad (9)$$

$$R^2 = 1 - \frac{\sum_{i=1}^N (y_i - \hat{y})^2}{\sum_{i=1}^N (y_i - \bar{y})^2} \quad (10)$$

where, N is the total number of datasets; y_i and \hat{y} represent the true value and prediction value of the i -th sample, respectively. \bar{y} represents the arithmetically mean of the data. When both MSE and MAE are smaller and R^2 approaches 1, the fitting error remains lower. The lower MSE and MAE value provide greater prediction accuracy.

3. Results and discussions

3.1. Phase evaluation and morphology analysis

Fig. 6 demonstrates the Scanning Electron Microscope (SEM) micrographs of electroless Ni–P and Ni–P–TiO₂ composite

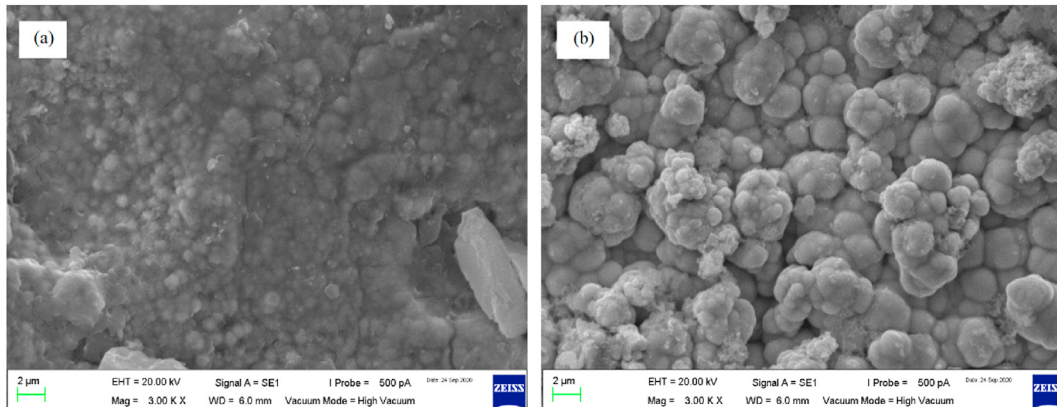


Fig. 6 – SEM images of (a) Ni–P and (b) Ni–P–TiO₂ coated substrate.

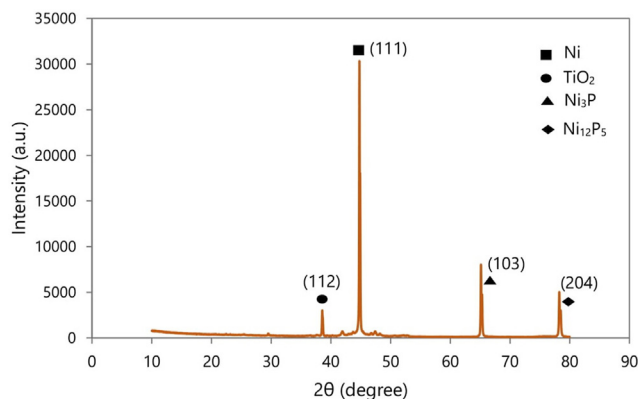
Table 3 – EDS results of electroless Ni–P and Ni–P–TiO₂ composite coating.

Coating	Composition (wt.%)					
	Ni	P	Ti	O	C	Al
Ni–P	83.8	4.9	—	4.5	5.9	0.9
Ni–P–TiO ₂	82.0	5.1	1.9	3.0	7.2	0.8

coating. The existence of micro-cracks and cavities was reported in the electroless Ni–P coated substrate (Fig. 6a), it was interpreted that some regions were not completely deposited by Ni–P particles. In the medium phosphorus content, the formation of Ni₃P and Ni₂P (brittle phase) emerges and the cracks propagate quickly in the brittle structure of the coated substrate where the amount of Ni₃P and Ni₂P (brittle phase) is maximum [63]. Another reason for developing microcracks and cavities is the generation of hydrogen gas and release of the hydrogen bubbles. It could be influenced by the effect of the competitive of the initial nucleation stage and lots of bubbles were released from the electrolyte due to the release of hydrogen [64]. The micrograph shows that Ni–P–TiO₂ coated substrate is uniform in shape and size (Fig. 6b). However, the agglomeration of spherical particles is found in some areas, and the film reveals no cracks and defects. It can be observed that, despite some of the nanoparticles being reunited, the Ni–P–TiO₂ composite coating exhibits a uniform distribution of TiO₂ nanoparticles on the coated surface compared with Ni–P coating. By incorporating TiO₂ nanoparticles in electroless Ni–P plating bath solution, it can hinder the plastic deformation of the composite coating matrix and thus improves the microhardness of the coated substrate.

Table 3 represents the chemical composition (wt.%) of coating deposits collected by EDS results. It can be reported that with the incorporation of TiO₂ nanoparticles, the phosphorus content increases from 4.9 wt.% to 5.1 wt.% and the Ni content decreases from 83.8 wt.% to 82.0 wt.%. The addition of TiO₂ nanoparticles is responsible for the change in the elemental composition (wt.%) of the nanocomposite coating. There has been a previous research showing that the reduction of particle size decreases the co-deposition content of the particles [65]. From XRD phase information, the crystallite size of Ni and TiO₂ was found to be 85.26 nm and 100.64 nm, respectively. Therefore, when TiO₂ nanoparticles are added into the Ni–P matrix, the weight percentage (wt.%) of Ni deposition on the substrate decreases slightly according to their crystallite size. The incorporation of TiO₂ nanoparticles into electrolyte increases the density of nucleation sites and to inhibit the crystal growth of Ni by changing Ni nucleation mechanism [66]. The low amount of TiO₂ nanoparticles deposition during the electroless Ni–P plating bath solution was verified by the elemental composition of titanium (1.9 wt.%) and oxygen (3.0 wt.%) found on the EDS spectrum.

Fig. 7 shows the XRD patterns of Ni–P–TiO₂ coated aluminium substrate. Both Ni and TiO₂ peaks are appeared in the pattern and Nickel-phosphide nanocrystals with different peaks are also observed, which confirm the deposition of electroless Ni–P–TiO₂ coating materials on aluminium substrate. The XRD patterns also confirmed the

**Fig. 7 – XRD pattern of electroless Ni–P–TiO₂ coated substrate.**

presence of the TiO₂ particles embedded into the Ni–P matrix. The XRD pattern of electroless Ni–P–TiO₂ composite coating shows a weaker TiO₂ peak than Ni peak due to low distribution of TiO₂ particles in electroless plating solution. The phases Ni (111) and TiO₂ (112) peaks were observed at a diffraction angle (2θ) = 44.79° and 38.55°, respectively. Some sharp peaks of Ni and Ni₃P phases are observed where Ni (111) peak reaches to the maximum and other phases have lower peaks compared to Ni. The presence of sharp diffraction peak is an indication of crystalline structure of Ni. In the face-centred cube crystal structure, Ni (111) face is a close-packed plane of atoms and this type of crystal structure has greater compact density [67]. Due to the greater compact density, the nanocomposite coated substrate shows higher microhardness.

The crystallite or grain size of different particles was calculated using the following Scherrer equation,

$$S = (0.94\lambda) / (\beta \cos\theta) \quad (11)$$

where S is the diameter of the crystallites, λ is the wavelength whose value is 0.1548, β denotes full width at half maximum and θ is the position angle. The value of these unknown parameters (β and θ) was collected by utilizing the XRD patterns and “X’Pert HighScore Plus” software. The crystallite size of the particles at the standard peaks were evaluated at different position angle. The mean crystallite size (diameter) of TiO₂ particles was found to be 100.64 nm, indicating that the coated TiO₂ layer has nanocrystalline nature.

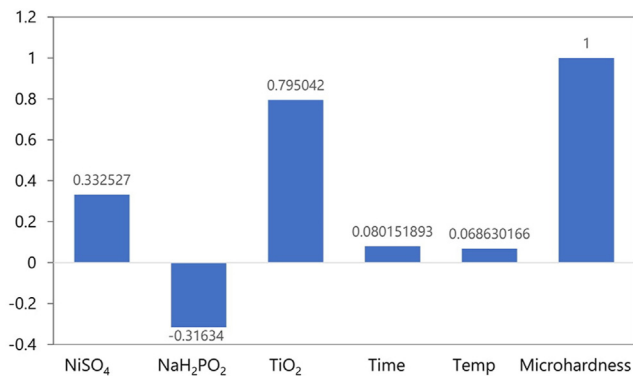
3.2. Data description

A set of statistical features was extracted from these process parameters along with response, including count, mean, maximum, minimum, and standard deviation as listed in Table 4.

From the analysis of Fig. 8 and Table 5, it is possible to determine which variables (NiSO₄, NaH₂PO₂, TiO₂, Time and Temperature) have the greatest impact on the microhardness. It can be evident that the parameter with the greatest influence on the microhardness is the concentration of TiO₂. The NiSO₄, TiO₂, time and temperature have a positive correlation with Vickers microhardness. Nevertheless, the correlation between NaH₂PO₂ and microhardness is negative, indicating that lowering the

Table 4 – Statistical description of process parameters and response.

	NiSO ₄	NaH ₂ PO ₂	TiO ₂	Time	Temperature	Microhardness
count	36	36	36	36	36	36
mean	45	32.5	2.333333	90	87.33333	168.1139
std	5.070926	2.535463	2.083952	24.84236	6.215189	43.52089
min	40	30	0	60	80	102.9
25%	40	30	0	60	80	129.1
50%	45	32.5	2	90	87	163.65
75%	50	35	5	120	95	198.525
max	50	35	5	120	95	278.6

**Fig. 8 – Correlation of the process parameters with microhardness.**

concentration of NaH₂PO₂ in electroless plating bath solution would result in increased microhardness. The sequence of the influenced parameter from high to low was obtained as follows: TiO₂ > NiSO₄ > NaH₂PO₂ > Time > Temperature.

3.3. RSM modelling

The RSM model for microhardness was developed by using experimental results through “Design-Expert” software. The suggested linear model in the fit summary was found to be the good starting point for model fitting based on Analysis of Variance (ANOVA) model. The result of ANOVA for the microhardness model will exhibit the key effect of the five process parameters (coating compositions and coating operational parameters).

3.3.1. ANOVA for response surface linear model

The ANOVA table for modelling of microhardness has been shown in Table 6. As demonstrated, the F-value of the model is 35.06 which implies that the generated model is significant. Due to noise, there is only a 0.01% probability that a “Model F-

value” this large could occur. The model P-value of 0.0001 implies that the model is significant. P-values over 0.10 imply that the terms of the model are not relevant. In this present ANOVA model, NiSO₄ (A), NaH₂PO₂ (B) and TiO₂ (C) exhibit notable model terms. ANOVA also explains the main effects of the parameters, their interactive behaviour and error terms present in the model.

3.3.2. Analysis of hardness effect on process variables

The response surface methodology can properly reflect each factor's ability to influence the microhardness. The highest F-value (129.77) for C variable (Table 6) amongst five process variables (A, B, C, D and E) implies that the TiO₂ concentration has the most significant influence on microhardness. However, the E variables (temperature) reveals the lowest impact on the response by showing the least F-value. Apart from the mathematical model, there is a pictorial diagram which can examine the effect of all variables at a given position in the design space. This pictorial diagram is known as perturbation graph. Fig. 9 illustrates the perturbation plot of the five process variables on the microhardness response. It can be observed that the microhardness decreases when the concentration of NaH₂PO₂ increases. However, for the rest of the process parameters microhardness increases at the increased value of the process parameters except NaH₂PO₂. It is also evident from Fig. 9 that, as opposed to other process variables, variables D and E (time and temperature) have less impact on microhardness.

Fig. 10 displays the graph of the experimental response and predicted response where horizontal axis represents the actual value and vertical axis shows the predicted response. The correlation between the actual value and expected response can be found at a satisfactory stage. No unexpected change of the continuous variance is reported in the model [68]. The actual data points in the graph are in close agreement with the anticipated ones, implying that the linear model is an efficient model for estimating the response of the

Table 5 – Correlation table.

	NiSO ₄	NaH ₂ PO ₂	TiO ₂	Time	Temperature	Micro-hardness
NiSO ₄	1					
NaH ₂ PO ₂	0	1				
TiO ₂	0	0	1			
Time	0	0	1.96E-18	1		
Temperature	0	0	3.92E-17	0	1	
Micro-hardness	0.332527	-0.31634	0.795042	0.080151893	0.068630166	1

Table 6 – Analysis of variance (ANOVA) table for microhardness model.

Source	Sum of Squares	df	Mean Square	F-value	p-value	
Model	56605.27	5	11321.05	35.06	<0.0001	significant
A–NiSO ₄	7330.21	1	7330.21	22.70	<0.0001	
B–NaH ₂ PO ₂	6634.10	1	6634.10	20.55	<0.0001	
C–TiO ₂	41902.83	1	41902.83	129.77	<0.0001	
D–Time	425.88	1	425.88	1.32	0.2599	
E–Temp.	312.24	1	312.24	0.9670	0.3333	
Residual	9687.09	30	322.90			
Lack of Fit	9687.09	24	403.63			
Pure Error	0.0000	6	0.0000			
Cor Total	66292.36	35				

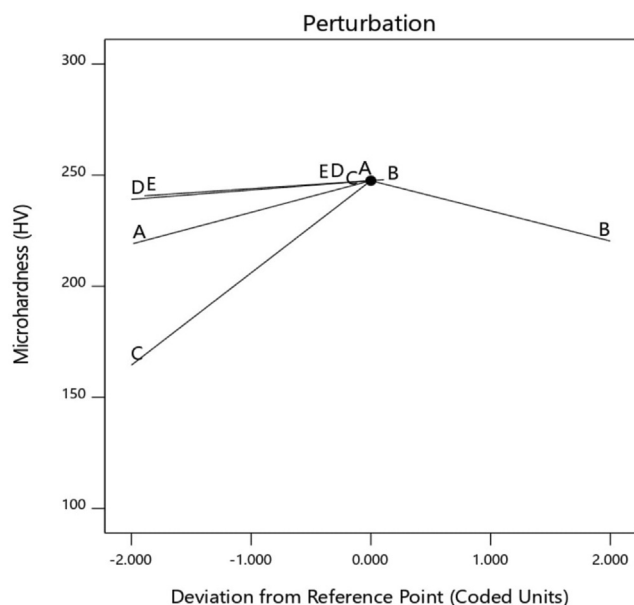
independent variable showing 269.084, 12.819 and 0.8539 for MSE, MAE and R² value, respectively (Table 7).

3.3.3. Optimization assessment for process variables

By using the numerical optimization feature of the “Design-Expert” software, the optimum conditions for the process parameter are predicted. As shown in Table 8, the different input restraints goals of process variables are selected to optimize the response. The optimum conditions for dependent variable were achieved by integrating the linear model prediction equation based on experimental results and response analysis of the surface plot. Table 9 represents the set of input parameters and the response with the optimum values obtained, where the corresponding desirability was 0.826 and 0.823 for the two proposed optimal solutions. The optimized maximum microhardness 247.959 HV can be achieved at a NiSO₄, NaH₂PO₂ and TiO₂ concentration of 49.993, 30.026 and 5.0 gm/L respectively with 119.94 min and 94.99 °C temperature.

The Final equation in terms of actual factors is given below.

$$\begin{aligned} \text{Microhardness} = & +122.81491 + 2.85389 \times \text{NiSO}_4 - 5.43000 \\ & \times \text{NaH}_2\text{PO}_2 + 16.60351 \times \text{TiO}_2 + 0.140417 \times \text{Time} \\ & + 0.480572 \times \text{Temp.} \end{aligned} \quad (12)$$

**Fig. 9 – Perturbation plot.**

By using Eq. (12), the desired microhardness value can be predicted. In terms of actual variables, the equation can be utilized to make predictions of the response for each factor at given levels.

As shown in Fig. 11, RSM provides the optimized input parameters array recommended to get maximum microhardness response of electroless Ni–P–TiO₂ composite coating. The response is illustrated by altering all input parameters across their range while maintaining the output factor microhardness at maximum. The 3D surface plots were employed to estimate the response surface. The effect of two process variables on the microhardness response set at the central point values is shown by each plot in the experimental study ranges. The 3D plot shown in Fig. 11a gives the effect of NiSO₄, NaH₂PO₂ and interaction on the response surface keeping the remaining parameters at their centre points. Microhardness was found to increase at a higher concentration of NiSO₄ of about 49.99 gm/L and lower concentration of NaH₂PO₂ of about 30.03 gm/L. Similarly, Fig. 11b and (c) represent the effect of NiSO₄, TiO₂ and NaH₂PO₂, TiO₂ respectively on microhardness response. It can be clearly observed from Fig. 11 that the high level of NiSO₄ and TiO₂ increases the microhardness value. On the other hand, high

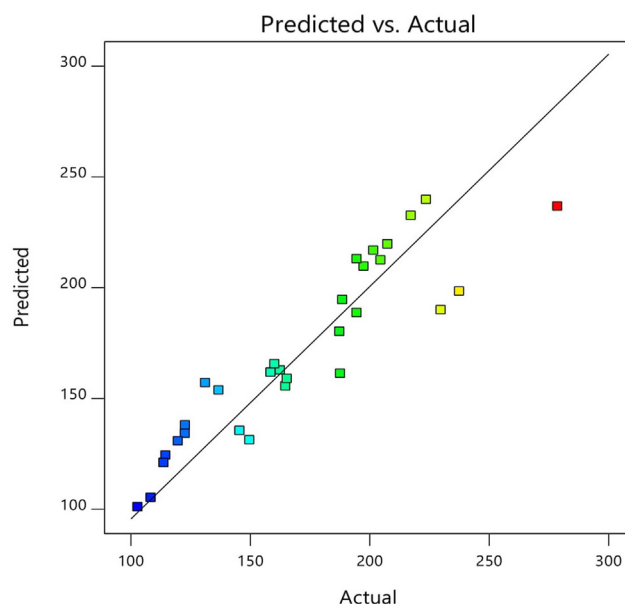
**Fig. 10 – Microhardness plot of predicted vs. actual for RSM model.**

Table 7 – RSM model evaluations of the performance metrics for microhardness.

Metric	Value
MSE	269.084
MAE	12.819
R ²	0.8539

level of NaH₂PO₂ concentration decreases the microhardness response. The orange-coloured region of the 3D response surface plot (Fig. 11) shows the maximum height of the plot and hence represents the highest value of the microhardness. The orange colour covered area is the region where optimized values can be obtained and predict the best microhardness value with respect to process parameters. The experimental results were further evaluated through machine learning algorithms (AI models) and compared with RSM model.

3.4. AI modelling

3.4.1. Parameter tuning of AI models

Parameter tuning for machine learning model is very essential to obtain desired results. On the basis of trial and error, the parameters were tuned in the best possible ways to obtain the best outcome from the four AI models studied in this manuscript.

For ANN, the network configuration for the prediction model is (5-8-8-1), where number of hidden layers are 2, number of nodes of hidden layers are 16, number of epochs are 1000 and validation split is 0.2. For input and hidden layer, ReLU (Rectified Linear Unit) was used as an activation function. On the other hand, sigmoid was used as a transfer function for the output. Sigmoid transfer function was used in this case because of its regression application.

In case of SVM, the best possible C parameter and gamma values were obtained through grid search regarding to the datasets. By utilizing grid search, C = 0.1 and gamma = 1 was determined.

The values of tuned parameters for random forest and extra trees models are almost similar except the *n_estimators* value. The parameter values for AI models have been shown in Table 10. The *random_state* ensures that the generated splits are reproducible. If *random_state* is not used in *train_test_split*,

every time it will give a different set of train and test data points and will not help in debugging issues. Although generating more trees give better results, it has some limitations. The time complexity of RF and ET models increases through the selection of a larger number of trees. Therefore, adequate *n_estimators* value is required for better results. The *max_depth* of a tree is considered as the lengthiest path between the leaf node and the root node. The parameter which informs the decision tree in AI models (RF and ET) to split the minimum number of observations needed in any given model is known as *min_sample_split*.

3.4.2. Model validation and prediction of microhardness based on AI models

The microhardness prediction framework was modelled with high precision using machine learning techniques without having to perform complicated experiments and mathematical operations. Four AI models (SVM, ANN, RF and ET) were applied in this study to predict microhardness and a comprehensive comparative analysis was also done between these models to verify their performance. In general, the training performance of the models depends on the dataset because they are under supervised learning algorithms. According to the No Free Lunch (NFL) theorem [69], it is not obvious in every dataset that the specific AI model will always work with high accuracy and precision. Therefore, the possible best four AI models have been considered and applied in this research. For training the AI models, 3 coating compositions (NiSO₄, NaH₂PO₂, TiO₂) and 2 coating operational parameters (time, temperature) were considered as input parameters while microhardness was regarded as the output parameter. The microhardness data samples were split into training data and testing data to verify the accuracy of the AI models. For the models, the whole dataset containing of 36 data samples was used, where 27 data samples (75%) were randomly selected as training samples, and the remainder 9 data samples (25%) were used as testing samples for output prediction assessment.

A glance at the (Figs. 12–14) reveal that ET model outperformed the SVM, ANN and RF models in terms of their performance parameters. The bar graphs show the mean square error (MSE) (Fig. 12) and mean absolute error (MAE)

Table 8 – Limits of input parameters with weight range.

Name	Goal	Lower Limit	Upper Limit	Lower Weight	Upper Weight	Importance
A: NiSO ₄	in range	40	50	1	1	3
B: NaH ₂ PO ₂	in range	30	35	1	1	3
C: TiO ₂	in range	0	5	1	1	3
D: Time	in range	60	120	1	1	3
E: Temp.	in range	80	95	1	1	3
Microhardness	maximize	102.9	278.6	1	1	3

Table 9 – Numerical optimization and desirability values.

Number	NiSO ₄ (gm/L)	NaH ₂ PO ₂ (gm/L)	TiO ₂ (gm/L)	Time (mint.)	Temp. (°C)	Microhardness (HV)	Desirability
1	49.993	30.026	5.000	119.942	94.991	247.959	0.826
2	49.769	30.002	4.998	119.992	95.000	247.428	0.823

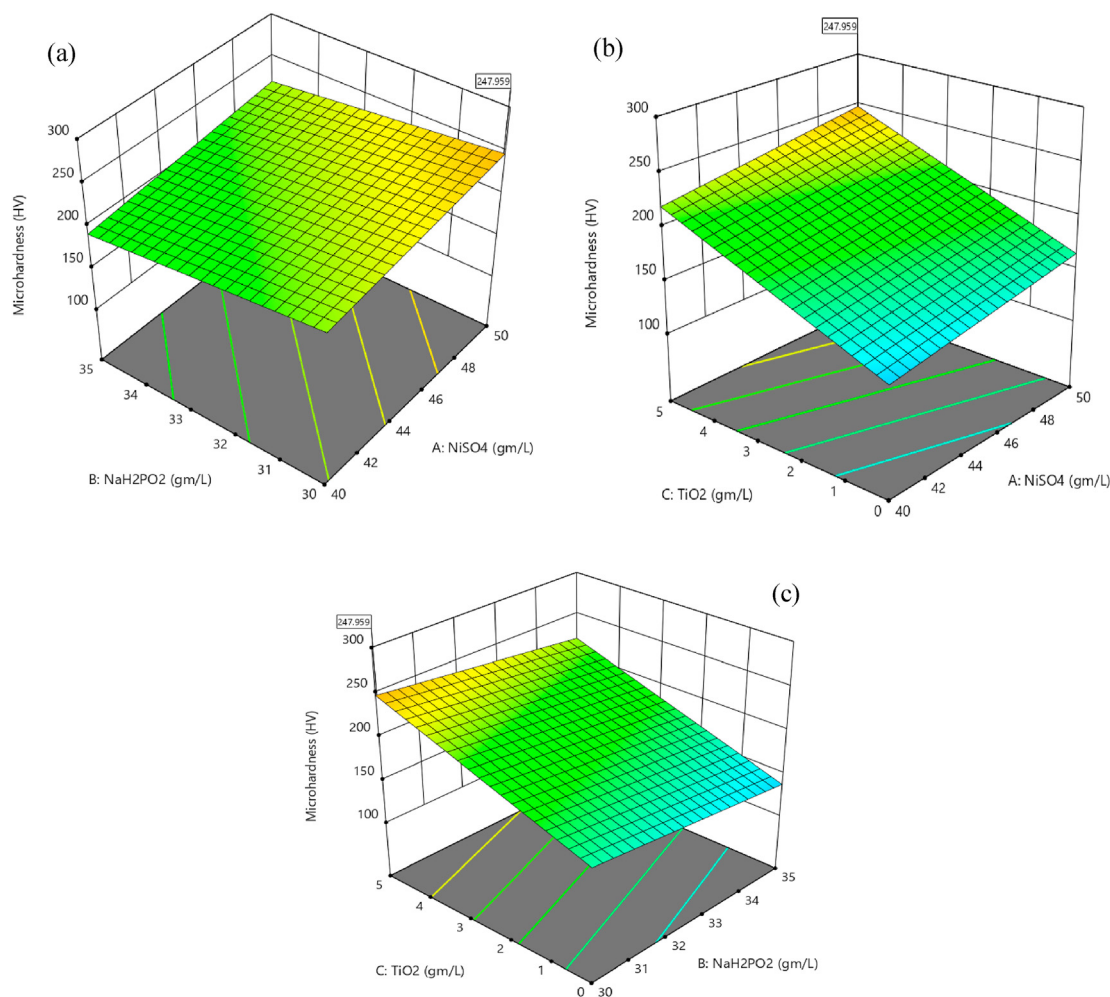


Fig. 11 – 3D Surface Plot showing the effect of (a) NiSO_4 and NaH_2PO_2 concentration (b) NiSO_4 and TiO_2 concentration (c) NaH_2PO_2 and TiO_2 concentration on microhardness response.

(Fig. 13) by performance categories (train, test, all) of AI models. The lower the MSE and MAE value, the better the AI models. As is observed from Figs. 12 and 13, in overall dataset, the MSE and MAE values of ET model are lower than other AI models. The SVM model possesses the highest MSE value in terms of training performance. Overfitting is observed in the SVM model, as a result a higher difference between training and testing dataset in case of MSE and MAE value was observed. Though the ANN model shows the highest error in training dataset, in overall extent it does not overfit like SVM model. However, the ANN model has struggled to produce accurate results due to its higher MSE values. The poor accuracy of the ANN model can be due to the limited ability of the ANN model to process large noises. The MSE value for the predictions of microhardness through RF model on the overall dataset shows lower error magnitude

than other two models (SVM and ANN). The RF model exhibits almost similar R^2 value to ET model. In case of MSE and MAE, ET outperformed other three AI models by providing the lowest error. ET model had the highest performance and predicted the microhardness with a R^2 value of 0.9447. The MSE and MAE values of the ET model were calculated as 75.384 and 4.679, respectively. The MSE and MAE values of the ET model are very small, implying no significant overestimation or underestimation of the target values and provides higher accuracy. As a result of this study, it was seen that the use of ET model for predicting the microhardness of electroless Ni–P– TiO_2 coating based on MAE value gives lower error rate of 26.18%, 38.26%, 60.34% than SVM, RF and ANN models, respectively. Therefore, in case of prediction accuracy the best to good AI model is as follows: ET, RF, ANN and SVM.

Table 10 – Parameter values of RF and ET models.

AI model	AI parameters				
	random_state	n_estimators	max_depth	min_sample_split	verbose
Random Forest	0	7	4	2	0
Extra trees	0	8	4	2	—

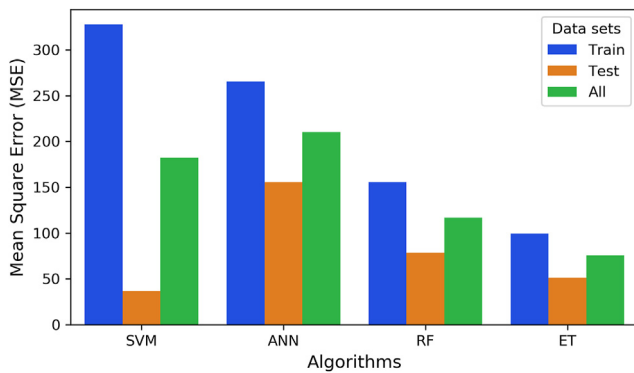


Fig. 12 – Mean Squared Error (MSE) of four AI models.

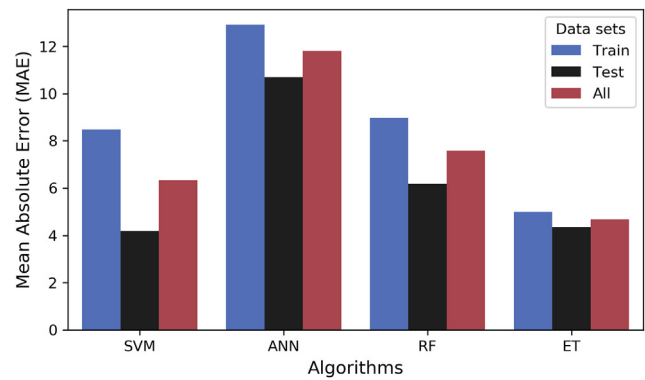


Fig. 13 – Mean Absolute Error (MAE) of four AI models.

The ET model estimated the R^2 value at 0.944728 and shows 3.02% better results than RF, which has the closest R^2 value. Results show that the ET method also performs better in terms of error (MSE and MAE) values with respect to other AI models. ET model provides least error among all AI models as well as showing least overfitting tendency. Fig. 15 delineates the scatter plots both for training and testing results. The actual microhardness value attained from the Vickers microhardness tester is the abscissa (horizontal axis) for each figure whereas the ordinate (vertical axis) indicates the predicted value based on the SVM, ANN, RF and ET models. The silver-coloured oblique line is the true-prediction line where the predicted values are equal to the actual values. The points nearer to the silver diagonal line illustrate the best prediction accuracy. It can easily be observed from the scatter plots that the ET model (Fig. 15 g and h) shows smaller deviations from the silver diagonal line and therefore exhibits better results than all other models.

3.4.3. Comparison of all models based on performance metrics

The values of evaluation performance metrics of the machine learning AI models and RSM model have been shown in Table 11 to compare the effectiveness of the models and to prognosticate the microhardness. The results show that the R^2 value of the ET model is 0.9447 which is higher than those of the SVM, ANN, RF and RSM models. The MSE and MAE values of the ET model are 75.384 and 4.679, respectively which are smaller than the four other models. Though ANN model might be considered weaker than the RSM model based on the value of R^2 , it is still capable of producing less (MSE and MAE) error values than RSM model. The MSE and MAE for RSM model were 269.084 and 12.819 while for ANN model it was 210.434 and 11.804, respectively. Moreover, it was found that the RSM model exhibits almost three times more error (MSE and MAE) compared to ET model. This outcome indicates that there is a higher deviation to the prediction of RSM than that of other models. Thus, the prediction accuracy of RSM is regarded as the lowest amongst five models. These above results demonstrate the potential superiority of ET model amongst other models. ET model outperformed the other four models in terms of their performance evaluation metrics.

4. Conclusions

By utilizing RSM model and machine learning approaches, the microhardness predictions were achieved with higher accuracy and precision. The microhardness of the coated substrates was influenced by changing coating parameters. The sequence of the influenced parameters on microhardness from high to low was obtained as follows: $\text{TiO}_2 > \text{NiSO}_4 > \text{NaH}_2\text{PO}_2 > \text{Time} > \text{Temperature}$, in which all parameters except NaH_2PO_2 are positively associated to microhardness. Higher microhardness values were found at high concentrations of TiO_2 nanoparticles and NiSO_4 solution. On the other hand, low concentration of NaH_2PO_2 gives higher microhardness value. The lowest microhardness value was recorded as 102.9 HV and the highest microhardness value was measured as 278.6 HV with Vickers microhardness tester. The RSM and AI models were applied to optimize and predict the microhardness in aspect of the coating composition and coating operational parameters. Microhardness values of electroless Ni–P– TiO_2 coated substrate have been successfully predicted by models designed using SVM, ANN, RF, ET and RSM models. The obtained R^2 values were 0.8929, 0.8420, 0.9145, 0.9447 and 0.8539 for the SVM, ANN, RF, ET and RSM models, respectively where RF and ET models give pretty much similar value (closer to unity). It can be easily observed from the results that the ET model shows better accuracy than all other models in terms of analysing with performance parameters in predicting microhardness. With higher accuracy and precision, Extra trees (ET) machine

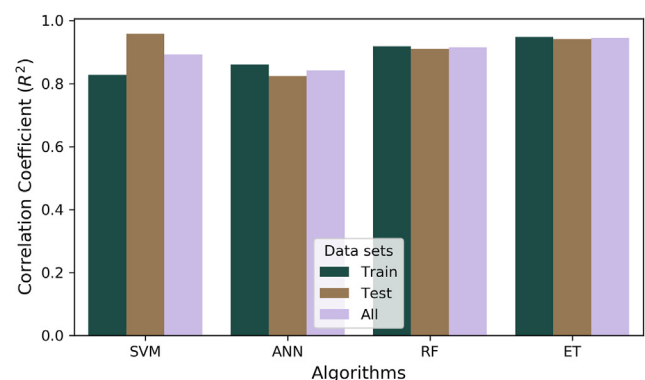


Fig. 14 – Correlation coefficient (R^2) of four AI models.

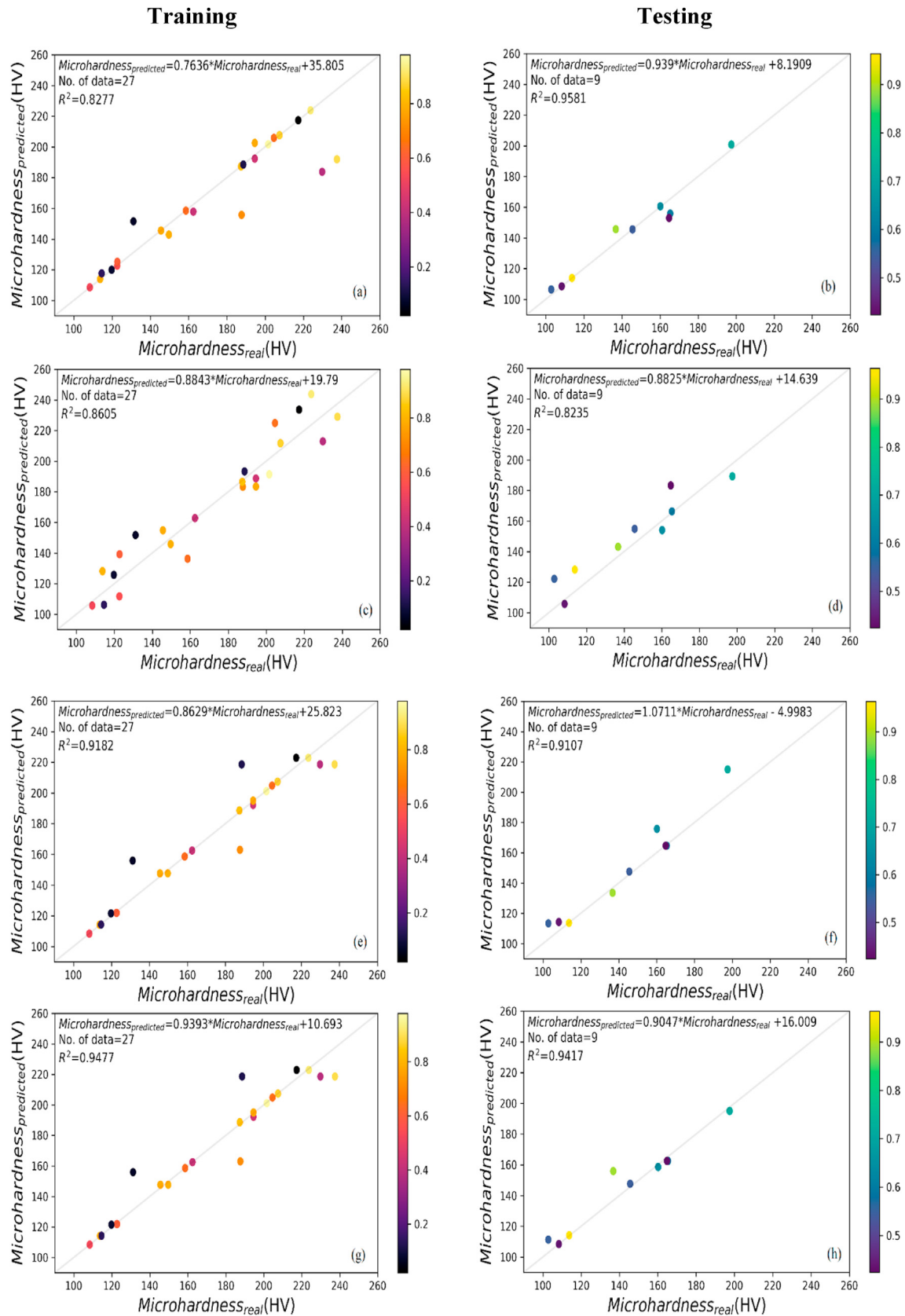


Fig. 15 – The actual vs predicted curve for microhardness for training and testing of SVM (a, b); ANN (c, d); RF (e, f) and ET (g, h) models.

Table 11 – Overall performance metrics of all AI models and RSM.

Models	MSE			MAE			R ²		
	Train	Test	All	Train	Test	All	Train	Test	All
SVM	327.5899	36.9792	182.2841	8.4850	4.1889	6.3370	0.8277	0.9581	0.8929
ANN	265.2052	155.6623	210.4337	12.9132	10.6939	11.8035	0.8605	0.8235	0.8420
RF	155.4733	78.7334	117.1034	8.9742	6.1868	7.5805	0.9182	0.9107	0.9145
ET	99.3530	51.4151	75.3840	5.0054	4.3535	4.6794	0.9477	0.9417	0.9447
RSM	–	–	269.084	–	–	12.819	–	–	0.8539

learning model can minimize the experimental complexities, time, and expense in the manufacture of parts with good surface properties by predicting microhardness. The approach given in this paper to the generated model and processing data is general, providing a new way to maximize the use of process parameters and establishing a strong indication of the further creation and application of electroless Ni–P–TiO₂ composite coating. The developed machine learning models along with RSM model can be further exploited in the fields of surface modification and materials industry without performing the complicated experiments and expensive tests.

Declaration of Competing Interest

The authors declare that they have no known competing financial interests or personal relationships that could have appeared to influence the work reported in this paper.

Acknowledgements

The authors thank the “Yayasan Universiti Teknologi PETRONAS (YUTP)” Research Fund (015LC0-238) for their financial contribution to this research.

REFERENCES

- [1] Abdel Aal A, Hassan HB, Abdel Rahim MA. Nanostructured Ni–P–TiO₂ composite coatings for electrocatalytic oxidation of small organic molecules. *J Electroanal Chem* 2008;619–620:17–25. <https://doi.org/10.1016/j.jelechem.2008.03.004>.
- [2] Alirezai S, Vaghefi SMM, Ürgen M, Saatchi A, Kazmanli K. Novel investigation on nanostructure Ni–P–Ag composite coatings. *Appl Surf Sci* 2012;261:155–8. <https://doi.org/10.1016/j.apsuc.2012.07.131>.
- [3] Ahmadkhaniha D, Eriksson F, Leisner P, Zanella C. Effect of SiC particle size and heat-treatment on microhardness and corrosion resistance of NiP electrodeposited coatings. *J Alloys Compd* 2018;769:1080–7. <https://doi.org/10.1016/j.jallcom.2018.08.013>.
- [4] Rabizadeh T, Allahkaram SR. Corrosion resistance enhancement of Ni–P electroless coatings by incorporation of nano-SiO₂ particles. *Mater Des* 2011;32:133–8. <https://doi.org/10.1016/j.matdes.2010.06.021>.
- [5] Balaraju JN, Selvi VE, Rajam KS. Electrochemical behaviour of high phosphorus electroless Ni–P–Si₃N₄ composite coatings. *Trans IMF* 2010;88:311–6. <https://doi.org/10.1179/002029610X12694310988928>.
- [6] León-Patiño CA, García-Guerra J, Aguilar-Reyes EA. Tribological characterization of heat-treated Ni–P and Ni–P–Al₂O₃ composite coatings by reciprocating sliding tests. *Wear* 2019;426–427:330–40. <https://doi.org/10.1016/j.wear.2019.02.015>.
- [7] Saravanan I, Elayaperumal A, Devaraju A, Karthikeyan M, Raji A. Wear behaviour of electroless Ni–P and Ni–P–TiO₂ composite coatings on En8 steel. *Mater Today Proc* 2020;22:1135–9. <https://doi.org/10.1016/j.matpr.2019.12.007>.
- [8] Shozib IA, Ahmad A, Majdi A, Tasnim N. Electroless Ni–P–TiO₂ (enpt) composite coating: a review on microstructural characteristics and multifarious properties for surgical instruments. *Solid State Technol* 2020;63:3989–96.
- [9] Chen W, Gao W, He Y. A novel electroless plating of Ni–P–TiO₂ nano-composite coatings. *Surf Coating Technol* 2010;204:2493–8. <https://doi.org/10.1016/j.surfcoat.2010.01.032>.
- [10] Yusuf NK, Lajis MA, Ahmad A. Hot press as a sustainable direct recycling technique of aluminium: mechanical properties and surface integrity. *Materials* 2017;10:902.
- [11] Haider K, Alam MA, Redhewal A, Saxena V. Investigation of mechanical properties of aluminium based metal matrix composites reinforced with sic & Al₂O₃. *Int J Eng Res Afr* 2015;5:63–9.
- [12] Cai J, Meyers MA, Jiang F, Vecchio KS, Nesterenko VF. Mechanical and microstructural properties of PTFE/Al/W system. *AIP conf. Proc.*, vol. 955. American Institute of Physics; 2007. p. 723–6.
- [13] Gerberich WW, Tymiak NI, Grunlan JC, Horstemeyer MF, Baskes MI. Interpretations of indentation size effects. *J Appl Mech* 2002;69:433–42. <https://doi.org/10.1115/1.1469004>.
- [14] George F, Voort V, Fowler R. Low-load Vickers microindentation hardness testing. *Adv Mater Process* 2012;170:28–33.
- [15] Sharma VK, Kumar V, Joshi RS. Parametric study of aluminium-rare earth based composites with improved hydrophobicity using response surface method. *J Mater Res Technol* 2020;9:4919–32. <https://doi.org/10.1016/j.jmrt.2020.03.011>.
- [16] Abu-Hamdeh NH, Golmohammadzadeh A, Karimipour A. Navigating viscosity of ferrofluid using response surface methodology and artificial neural network. *J Mater Res Technol* 2020;9:16339–48. <https://doi.org/10.1016/j.jmrt.2020.11.087>.
- [17] See TL, Zulkifli AZS, Tzeng LM. Application of Response Surface Methodology for characterization of ozone production from Multi-Cylinder Reactor in non-thermal plasma device. *IOP Conf Ser Mater Sci Eng* 2018;342:12087. IOP Publishing.
- [18] Sweetlana S, Khatavkar N, Singh AK. Development of Vickers hardness prediction models via microstructural analysis and machine learning. *J Mater Sci* 2020;55:15845–56. <https://doi.org/10.1007/s10853-020-05153-w>.
- [19] Wen C, Zhang Y, Wang C, Xue D, Bai Y, Antonov S, et al. Machine learning assisted design of high entropy alloys with desired property. *Acta Mater* 2019;170:109–17. <https://doi.org/10.1016/j.actamat.2019.03.010>.

- [20] Ward L, Liu R, Krishna A, Hegde VI, Agrawal A, Choudhary A, et al. Including crystal structure attributes in machine learning models of formation energies via Voronoi tessellations. *Phys Rev B* 2017;96:24104.
- [21] Juneja R, Yumnam G, Satsangi S, Singh AK. Coupling the high-throughput property map to machine learning for predicting lattice thermal conductivity. *Chem Mater* 2019;31:5145–51.
- [22] Jha A, Chandrasekaran A, Kim C, Ramprasad R. Impact of dataset uncertainties on machine learning model predictions: the example of polymer glass transition temperatures. *Model Simulat Mater Sci Eng* 2019;27:24002.
- [23] Huang W, Martin P, Zhuang HL. Machine-learning phase prediction of high-entropy alloys. *Acta Mater* 2019;169:225–36. <https://doi.org/10.1016/j.actamat.2019.03.012>.
- [24] Ulas M, Aydur O, Gurgenc T, Ozel C. Surface roughness prediction of machined aluminum alloy with wire electrical discharge machining by different machine learning algorithms. *J Mater Res Technol* 2020;9:12512–24. <https://doi.org/10.1016/j.jmrt.2020.08.098>.
- [25] Liu Y, Zhao T, Ju W, Shi S. Materials discovery and design using machine learning. *J Mater* 2017;3:159–77. <https://doi.org/10.1016/j.jmat.2017.08.002>.
- [26] Yating W, Bin S, Lei L, Wenbin H. Artificial neural network modelling of plating rate and phosphorus content in the coatings of electroless nickel plating. *J Mater Process Technol* 2008;205:207–13. <https://doi.org/10.1016/j.jmatprotec.2007.11.095>.
- [27] Beygi H, Vafaenezhad H, Sajjadi SA. Modeling the electroless nickel deposition on aluminum nanoparticles. *Appl Surf Sci* 2012;258:7744–50. <https://doi.org/10.1016/j.apsusc.2012.04.132>.
- [28] Vaghefi SYM, Vaghefi SMM. Prediction of phosphorus content of electroless nickel–phosphorous coatings using artificial neural network modeling. *Neural Comput Appl* 2011;20:1055–60.
- [29] Zou XF, Hu YJ, Long XB, Huang LY. Prediction and optimization of phosphorus content in electroless plating of Cr12MoV die steel based on PSO-BP model. *Surfaces and Interfaces* 2020;18:100443.
- [30] Gadhari P, Sahoo P. Optimization of coating process parameters to improve microhardness of Ni–P–TiO₂ composite coatings. *Mater Today Proc* 2015;2:2367–74. <https://doi.org/10.1016/j.matpr.2015.07.303>.
- [31] Sarkar S, Baranwal RK, Biswas C, Majumdar G, Haider J. Optimization of process parameters for electroless Ni–Co–P coating deposition to maximize micro-hardness. *Mater Res Express* 2019;6:46415.
- [32] Gadhari P, Sahoo P. Study of hardness and corrosion resistance of electroless Ni–P–TiO₂ composite coatings. *Int J Surf Eng Interdiscipl Mater Sci* 2015;3:18–40.
- [33] Alam MA, Ya HH, Azeem M, Hussain P Bin, bin Salit MS, Khan R, et al. Modelling and optimisation of hardness behaviour of sintered Al/SiC composites using RSM and ANN: a comparative study. *J Mater Res Technol* 2020;9:14036–50. <https://doi.org/10.1016/j.jmrt.2020.09.087>.
- [34] Muthukrishnan N, Davim JP. Optimization of machining parameters of Al/SiC–MMC with ANOVA and ANN analysis. *J Mater Process Technol* 2009;209:225–32. <https://doi.org/10.1016/j.jmatprotec.2008.01.041>.
- [35] Vitry V, Bonin L. Effect of temperature on ultrasound-assisted electroless nickel–boron plating. *Ultrason Sonochem* 2019;56:327–36. <https://doi.org/10.1016/j.jultsonch.2019.04.027>.
- [36] Sudagar J, Lian J, Sha W. Electroless nickel, alloy, composite and nano coatings – a critical review. *J Alloys Compd* 2013;571:183–204. <https://doi.org/10.1016/j.jallcom.2013.03.107>.
- [37] Gadhari P, Sahoo P. Study of wear behavior of Ni–P–TiO₂ composite coatings by optimizing coating parameters. *Mater Today Proc* 2017;4:1883–92. <https://doi.org/10.1016/j.jmrt.2017.02.033>.
- [38] Tamilarasan TR, Rajendran R, Rajagopal G, Sudagar J. Effect of surfactants on the coating properties and corrosion behaviour of Ni–P–nano-TiO₂ coatings. *Surf Coating Technol* 2015;276:320–6. <https://doi.org/10.1016/j.surfcoat.2015.07.008>.
- [39] Sankara Narayanan TSN, Baskaran I, Krishnaveni K, Parthiban S. Deposition of electroless Ni–P graded coatings and evaluation of their corrosion resistance. *Surf Coating Technol* 2006;200:3438–45. <https://doi.org/10.1016/j.surfcoat.2004.10.014>.
- [40] Salcedo-Sanz S, Rojo-Álvarez JL, Martínez-Ramón M, Camps-Valls G. Support vector machines in engineering: an overview. *Wiley Interdiscip Rev Data Min Knowl Discov* 2014;4:234–67.
- [41] Huang SH, Zhang H-C. Artificial neural networks in manufacturing: concepts, applications, and perspectives. *IEEE Trans Compon Packag Manuf Technol* 1994;17:212–28. <https://doi.org/10.1109/95.296402>.
- [42] Nwobi-Okoye CC, Ochizee BQ, Okiy S. Multi-objective optimization and modeling of age hardening process using ANN, ANFIS and genetic algorithm: results from aluminum alloy A356/cow horn particulate composite. *J Mater Res Technol* 2019;8:3054–75. <https://doi.org/10.1016/j.jmrt.2019.01.031>.
- [43] Tkáč M, Verner R. Artificial neural networks in business: two decades of research. *Appl Soft Comput* 2016;38:788–804. <https://doi.org/10.1016/j.asoc.2015.09.040>.
- [44] Paturi UMR, Cheruku S, Geerreddy SR. Process modeling and parameter optimization of surface coatings using artificial neural networks (ANNs): state-of-the-art review. *Mater Today Proc* 2020. <https://doi.org/10.1016/j.matpr.2020.08.695>.
- [45] Ghritlahre HK, Prasad RK. Application of ANN technique to predict the performance of solar collector systems - a review. *Renew Sustain Energy Rev* 2018;84:75–88. <https://doi.org/10.1016/j.jrser.2018.01.001>.
- [46] Teodosiu C, Pastravanu O, Macoveanu M. Neural network models for ultrafiltration and backwashing. *Water Res* 2000;34:4371–80. [https://doi.org/10.1016/S0043-1354\(00\)00217-7](https://doi.org/10.1016/S0043-1354(00)00217-7).
- [47] Mohammed A, Rafiq S, Sihag P, Kurda R, Mahmood W, Ghafor K, et al. ANN, MSP-tree and nonlinear regression approaches with statistical evaluations to predict the compressive strength of cement-based mortar modified with fly ash. *J Mater Res Technol* 2020;9:12416–27. <https://doi.org/10.1016/j.jmrt.2020.08.083>.
- [48] Maheshwera Reddy Paturi U, Devarasetti H, Kumar Reddy Narala S. Application of regression and artificial neural network analysis in modelling of surface roughness in hard turning of AISI 52100 steel. *Mater Today Proc* 2018;5:4766–77. <https://doi.org/10.1016/j.matpr.2017.12.050>.
- [49] Hitziger M, Ließ M. Comparison of three supervised learning methods for digital soil mapping: application to a complex terrain in the Ecuadorian Andes. *Appl Environ Soil Sci* 2014;2014.
- [50] Jamson AH, Merat N, Carsten OMJ, Lai FCH. Behavioural changes in drivers experiencing highly-automated vehicle control in varying traffic conditions. *Transport Res C Emerg Technol* 2013;30:116–25.
- [51] Butler KT, Davies DW, Cartwright H, Isayev O, Walsh A. Machine learning for molecular and materials science. *Nature* 2018;559:547–55. <https://doi.org/10.1038/s41586-018-0337-2>.
- [52] Papadopoulos S, Azar E, Woon W-L, Kontokosta CE. Evaluation of tree-based ensemble learning algorithms for

- building energy performance estimation. *J Build Perform Simul* 2018;11:322–32.
- [53] McWilliams CJ, Lawson DJ, Santos-Rodriguez R, Gilchrist ID, Champneys A, Gould TH, et al. Towards a decision support tool for intensive care discharge: machine learning algorithm development using electronic healthcare data from MIMIC-III and Bristol, UK. *BMJ Open* 2019;9:e025925.
- [54] Hajjem A, Bellavance F, Larocque D. Mixed-effects random forest for clustered data. *J Stat Comput Simulat* 2014;84:1313–28.
- [55] Breiman L. Random forests. *Mach Learn* 2001;45:5–32.
- [56] Rachman A, Ratnayake RMC. Machine learning approach for risk-based inspection screening assessment. *Reliab Eng Syst Saf* 2019;185:518–32. <https://doi.org/10.1016/j.res.2019.02.008>.
- [57] Zhang C, Ma Y. Ensemble machine learning: methods and applications. Springer; 2012.
- [58] Ahmad MW, Mourshed M, Rezgui Y. Trees vs Neurons: comparison between random forest and ANN for high-resolution prediction of building energy consumption. *Energy Build* 2017;147:77–89. <https://doi.org/10.1016/j.enbuild.2017.04.038>.
- [59] Geurts P, Ernst D, Wehenkel L. Extremely randomized trees. *Mach Learn* 2006;63:3–42.
- [60] John V, Liu Z, Guo C, Mita S, Kidono K. Real-time lane estimation using deep features and extra trees regression. In: *Image video technol*. Springer; 2015. p. 721–33.
- [61] Wehenkel L, Ernst D, Geurts P. Ensembles of extremely randomized trees and some generic applications. *Proc Robust Methods Power Syst State Estim Load Forecast* 2006.
- [62] Seyyedattar M, Ghiasi MM, Zendejboudi S, Butt S. Determination of bubble point pressure and oil formation volume factor: extra trees compared with LSSVM-CSA hybrid and ANFIS models. *Fuel* 2020;269:116834. <https://doi.org/10.1016/j.fuel.2019.116834>.
- [63] Hadipour A, Monirvaghefi S M, Bahrololoom ME. Electroless deposition of graded Ni–P coatings. *Surf Eng* 2015;31:399–405.
- [64] Wu W, Jiang J. Effect of plating temperature on electroless amorphous Ni–P film on Si wafers in an alkaline bath solution. *Appl Nanosci* 2017;7:325–33.
- [65] Wang S-C, Wei W-CJ. Kinetics of electroplating process of nano-sized ceramic particle/Ni composite. *Mater Chem Phys* 2003;78:574–80. [https://doi.org/10.1016/S0254-0584\(01\)00564-8](https://doi.org/10.1016/S0254-0584(01)00564-8).
- [66] Benea L, Danaila E. Nucleation and growth mechanism of Ni/TiO₂ nanoparticles electro-codeposition. *J Electrochem Soc* 2016;163:D655.
- [67] Momenzadeh M, Sanjabi S. The effect of TiO₂ nanoparticle codeposition on microstructure and corrosion resistance of electroless Ni₈ff; P coating. *Mater Corros* 2012;63:614–9.
- [68] Hafeez A, Ammar Taqvi SA, Fazal T, Javed F, Khan Z, Amjad US, et al. Optimization on cleaner intensification of ozone production using artificial neural network and response surface methodology: parametric and comparative study. *J Clean Prod* 2020;252:119833. <https://doi.org/10.1016/j.jclepro.2019.119833>.
- [69] Adam SP, Alexandropoulos S-AN, Pardalos PM, Vrahatis MN. No free lunch theorem: a review. *Approx. Optim.* Springer; 2019. p. 57–82.